Spin-label EPR Approaches to Protein Interactions

Son, M. van

1

INTRODUCTION

In 2014, the Protein Data Bank (PDB) reached the milestone of containing 100,000 biomolecular structures in its data base[1]. The fundament for this affluence has been laid in the early 1950s, when the first structures of the α-helix and β-sheet[2], the coiled-coil motif[3], and DNA[4;5] were reported. The large majority of the structures in the PDB were elucidated with X-ray crystallography, which even today remains the most common tool to determine biomolecular structure. This technique allows biomolecules to be studied at atomic detail, which has immensely enhanced our understanding of molecular biology.

X-ray crystallography provides only a static picture of the biomolecules, whose nature is essentially dynamic, and whose flexibility is closely related to their biological function. Think about the dynamics involved in processes such as protein folding, enzymatic reactions, or interacting proteins that facilitate membrane fusion and electron transfer. Methods other than X-ray crystallography are needed to study the dynamics of these biomolecules, to obtain information that goes beyond the static picture.

Electron paramagnetic resonance (EPR) spectroscopy[6] is well suited for providing such information and is sufficiently sensitive to characterize large biomolecular complexes. Distances of a few nanometres, corresponding to the

typical size of biomacromolecules, are accessible and EPR is able to deal with complex structures and high molecular weights. Furthermore, the application does not require that the molecules of interest are crystallized, which for many biomolecules and complexes is not feasible.

To use EPR, the biomolecule of interest must contain an unpaired electron – a requirement that is not met by all molecules. A paramagnetic centre, however, can be introduced by a nitroxide spin label.

1.1 Spin labelling

The spin-labelling technique[7-9] allows a spin label to be introduced at a particular position in the biomolecule. Figure 1.1 shows the chemical structure of the two spin labels used in this work: *S*-(1-oxyl-2,2,5,5-tetramethyl-2,5-dihydro-1H-pyrrol-3-yl)methyl methanesulfonothioate (MTSL)[10] and the alpha-amino acid 2,2,6,6-tetramethyl-piperidine-1-oxyl-4-amino-4-carboxylic acid (TOAC)[11].

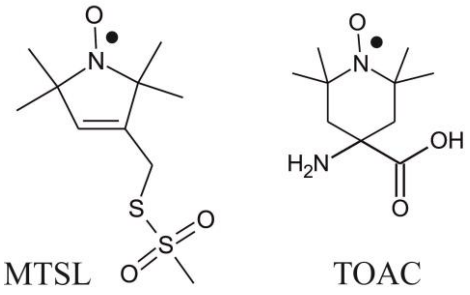

Figure 1.1 The chemical structures of the spin labels *S*-(1-oxyl-2,2,5,5-tetramethyl-2,5-dihydro-1H-pyrrol-3-yl) methyl methanesulfonothioate (MTSL), and alpha-amino acid 2,2,6,6-tetramethyl-piperidine-1-oxyl-4-amino-4-carboxylic acid (TOAC). Both spin labels have an unpaired electron (indicated by a dot) located at the N–O bond.

Owing to its convenience and chemical stability, the MTSL label has become the most widely used spin label for characterizing nanosecond motions[12], for determining distances[13], and for mapping protein topology[14]. The five-membered nitroxide ring is covalently coupled via the disulphide bond to a cysteine. A great advantage is gained when combined with mutagenesis. This allows a cysteine to be introduced at a selected position in a peptide or protein, thereby giving numerous possibilities to introduce the MTSL label into the biomolecule. This technique, known as site-directed spin labelling (SDSL)[15], has become a powerful tool for probing structure and dynamics of both water-soluble and membrane proteins of arbitrary molecular weight[14]. The five bonds that connect the ring of MTSL to the protein backbone are somewhat of a disadvantage, because they introduce additional degrees of motional freedom. Consequently, translating interspin-distance measurements and spatial-orientation information into structural constraints is challenging.

The TOAC label is an unnatural amino acid, which can be incorporated into peptides during synthesis. The six-membered nitroxide ring is rigid and directly fused to the peptide backbone. Hence, the nanosecond motions detected with EPR can be directly related to the peptide mobility. Unlike MTSL, the TOAC label cannot be easily incorporated into selected sites of proteins.

1.2 EPR principles

The spin of an unpaired electron has two, degenerate states. When an external magnetic field $\vec{B}$ is applied, the energy levels for these states are split due to the interaction of the spin with the field. This is called the Zeeman interaction, named after the Nobel laureate Pieter Zeeman. In 1896, he discovered the effect

of a strong magnetic field on the electromagnetic spectrum emitted by sodium[16].

We shall consider an electron spin, which interacts with a magnetic field, and has a hyperfine coupling (*hf*) with one neighbouring nuclear spin. Then, the spin Hamiltonian is

$$\mathcal{H} = \mathcal{H}_Z + \mathcal{H}_{hf} = \mu_B \vec{B} \cdot \vec{\vec{g}} \cdot \vec{S} + \vec{S} \cdot \vec{\vec{A}} \cdot \vec{I} , \qquad (1.1)$$

where μ_B is the Bohr magneton, $\vec{\vec{g}}$ is the *g* tensor, $\vec{S}$ is the electron spin angular momentum operator, $\vec{\vec{A}}$ is the hyperfine tensor, and $\vec{I}$ is the nuclear spin angular momentum operator. The tensors $\vec{\vec{g}}$ and $\vec{\vec{A}}$ are diagonal in the principal-axes system. The principal axes coincide with the molecular axes of the spin label as defined in Figure 1.2. For a nitroxide spin label, typical tensors are $\vec{\vec{g}} = (g_{xx}, g_{yy}, g_{zz})$ = (2.0088, 2.0061, 2.0027) and $\vec{\vec{A}} = (A_{xx}, A_{yy}, A_{zz})$ = (16, 15, 104) MHz.

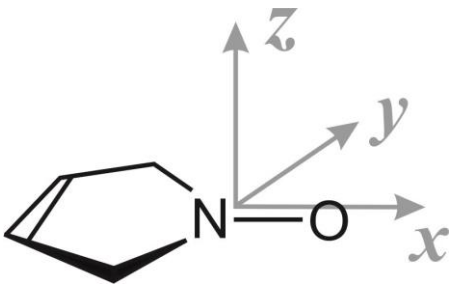

Figure 1.2 The molecular axes of the spin label MTSL. Only the ring structure including the nitroxide is shown. The *x*-axis coincides with the N─O bond, the *z*-axis is perpendicular to the ring.

To elaborate on the spin Hamiltonian in equation 1.1, two time regimes are distinguished: fast and slow molecular tumbling. Molecular tumbling is quantified in terms of the rotation-correlation time τ_r, which is the time a

molecule takes to rotate over one radian. Whether molecular tumbling is *fast* or *slow* depends on the value of τ_r with respect to the time scale of the EPR experiment.

Solution spectra – fast molecular tumbling

In the regime of fast tumbling, the molecular reorientations average out the anisotropic terms in equation 1.1. With

$$g = \tfrac{1}{3}\mathrm{Tr}\,\vec{\vec{g}} \qquad \text{and} \qquad a = \tfrac{1}{3}\mathrm{Tr}\,\vec{\vec{A}}, \tag{1.2}$$

the spin Hamiltonian has the isotropic form

$$\mathcal{H}_0 = g\mu_B \vec{B}\cdot\vec{S} + a\vec{S}\cdot\vec{I}. \tag{1.3}$$

Let the magnetic field have magnitude B and be directed along the molecular *z*-axis defined by the *g* tensor. Omitting the non-secular terms, equation 1.3 becomes

$$\mathcal{H}_0 = g\mu_B B S_z + a S_z I_z, \tag{1.4}$$

where S_z and I_z are the *z*-components of $\vec{S}$ and $\vec{I}$, respectively. The corresponding energy levels of the electron spin are

$$E(m_s, m_i) = g\mu_B B m_s + a m_s m_i, \tag{1.5}$$

where m_s is the eigenvalue of S_z (for the electron spin: $m_s = \pm\frac{1}{2}$) and m_i is the eigenvalue of I_z. A transition between the states occurs through absorption of microwaves whose frequency matches the energy difference. Satisfying the selection rules $\Delta m_s = \pm 1$ and $\Delta m_i = 0$, the resonance condition is met when

$$h\nu = g\mu_B B_0 + a m_i , \tag{1.6}$$

where h is Planck's constant and ν is the frequency of the microwaves. The nitroxide spin labels used in this work (Figure 1.1), have the electron spin coupled to the nuclear spin of ^{14}N, for which I = 1, with the corresponding eigenvalues $m_i = -1,\ 0,\ +1$. For the electron spin of a nitroxide, a schematic energy diagram is shown in Figure 1.3, with the allowed EPR transitions indicated by grey arrows.

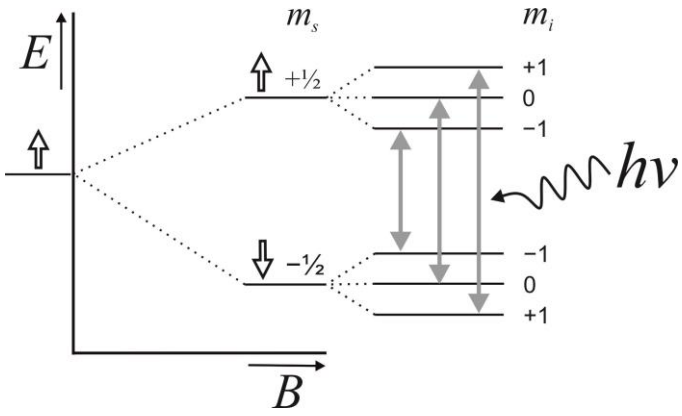

Figure 1.3 Schematic energy diagram of an electron spin $(S = ½)$ interacting with an external magnetic field and with a ^{14}N nuclear spin $(I = 1)$. The grey arrows indicate the transitions between the magnetic sublevels, which are induced by microwaves ($h\nu$), satisfying the selection rules $\Delta m_s = \pm 1$ and $\Delta m_i = 0$.

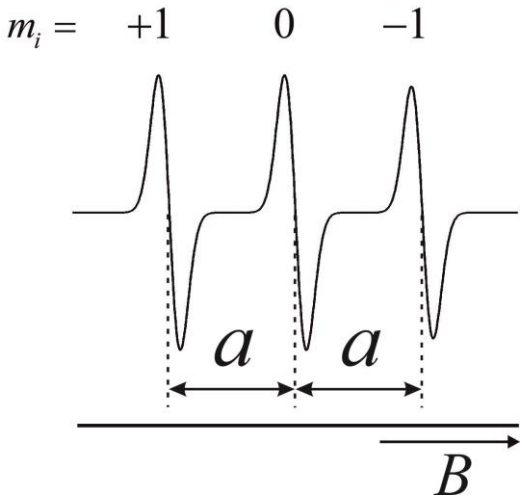

Figure 1.4 An example of a three-line EPR spectrum, which is typical for a nitroxide measured in cw mode. The lines are assigned to $m_i = +1,\ 0, -1$, and are spaced by the isotropic hyperfine coupling constant a.

Figure 1.4 shows an example of a three-line EPR spectrum, which is typical for a fast tumbling nitroxide measured in continuous wave (cw). The lines are designated with $m_i = +1,\ 0$, and -1, corresponding to the ^{14}N nuclear spin states, which split the electron spin states into three sublevels. As indicated in Figure 1.4, the isotropic hyperfine coupling a can be determined directly from the EPR spectrum.

Solution spectra – slow molecular tumbling

The spin Hamiltonian in equation 1.1 can be considered as the sum of two parts: the isotropic $\mathcal{H}_0$ (given in equation 1.3) and a purely anisotropic $\mathcal{H}_1$, which can be written as

$$\mathcal{H}_1 = \mu_B \vec{B} \cdot \vec{\vec{g}}' \cdot \vec{S} + \vec{S} \cdot \vec{\vec{A}}' \cdot \vec{I} \,. \qquad (1.7)$$

Here, $\vec{\vec{g}}'$ and $\vec{\vec{A}}'$ are traceless tensors. In solution, the molecular motions make $\mathcal{H}_1$ a random function of time. In spite of the vanishing average value of $\mathcal{H}_1$, broadening of the lines is expected to occur. The variations in linewidths and field positions, observed in solution spectra, derive from the fluctuations of the anisotropic terms of $\mathcal{H}_1$ by molecular motions.

The decisive effect of slow molecular tumbling on solution spectra is illustrated in Figure 1.5. Here, twelve simulated spectra show the rich variety in width and position of lines one would observe for different values of τ_r. The spectra were simulated at 9.8 GHz, 94 GHz, and 275 GHz, which are the experimental EPR frequencies available at Leiden Institute of Physics. In these simulations we assume τ_r to be isotropic, i.e., $\tau_{xx} = \tau_{yy} = \tau_{zz}$. The isotropic τ_r-values were set to 0.2 ns, 1 ns, 3 ns, and 10 ns at each of the microwave frequencies. Such simulations show that the anisotropy of $\vec{\vec{g}}$ becomes more apparent towards higher frequencies. Figure 1.6 shows that simulations at 94 GHz are also sensitive to the anisotropy in τ_r.

Software programs are available that enable the quantification of τ_r by fitting and/or simulating the cw-EPR spectrum. For example, Multicomponent[17] uses the stochastic Liouville approach based on the program of Freed et al.[18] for nitroxides in the slow-motion regime. The program EasySpin[19] is more elaborate than Multicomponent, for it calculates the spin Hamiltonian for a broader range of paramagnetic species and in different motional regimes.

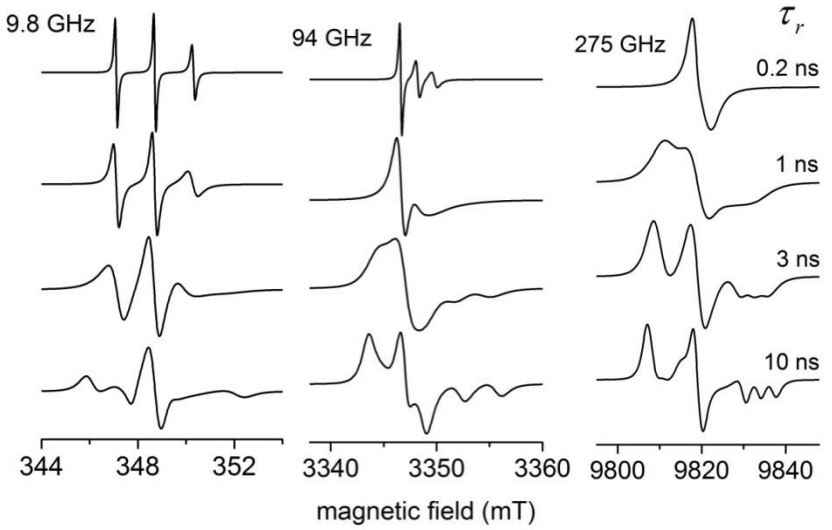

Figure 1.5 Simulations of EPR spectra in the regime of slow molecular tumbling with isotropic values for τ_r. The spectra show the effect of different values for τ_r (0.2, 1, 3, and 10 ns) on the width and position of lines for three microwave frequencies: 9.8, 94.0, and 275.7 GHz. All simulations were done using the EasySpin software package[19] with the algorithm *Chili*, using a Lorentzian linewidth of 0.1 mT, a hyperfine coupling of $[A_{xx}\ A_{yy}\ A_{zz}]$ = [16.0 15.0 104.1] MHz, and a g tensor of $[g_{xx}\ g_{yy}\ g_{zz}]$ = [2.0088 2.0061 2.0027].

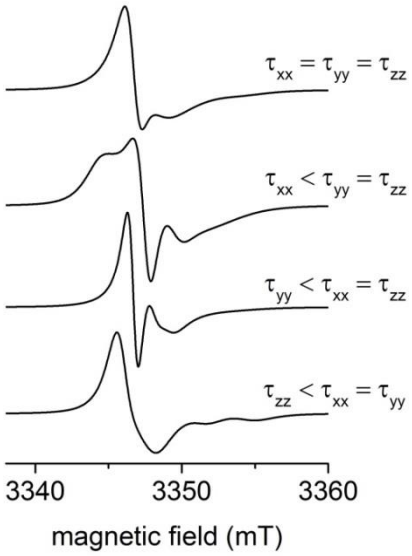

Figure 1.6 Simulations of EPR spectra at 94.0 GHz in the regime of slow molecular tumbling with anisotropic values for τ_r. The bottom three spectra represent results with one fast component (0.7 ns) and two slow components (2.8 ns). For comparison, the top spectrum was simulated with an isotropic τ_r of 1.4 ns. The other simulation parameters used were as mentioned in the caption of Figure 1.5.

1.3 Relaxation of electron spins

The population of the levels $m_s = +\frac{1}{2}$ and $m_s = -\frac{1}{2}$ is governed by the Boltzmann distribution. At room temperature, the difference between the populations is very small, since the magnetic energy is much smaller than the thermal energy. Nevertheless, this difference is responsible for the detection of the EPR signal. The absorption of microwaves can equalize the population of the magnetic levels, causing the EPR signal to disappear. Relaxation, however, brings the system back to the Boltzmann populations and allows for a continuous detection of the EPR signal.

Longitudinal and transverse relaxation, T_1 and T_2

In the presence of an external magnetic field aligned along the *z*-axis, a collection of spins has at thermal equilibrium a bulk magnetization vector $\vec{\mathrm{M}}$ directed along the *z*-axis. When $\vec{\mathrm{M}}$ is perturbed, longitudinal relaxation causes $\vec{\mathrm{M}}$ to be restored along the *z*-axis. This process involves a loss of magnetic energy, which is dissipated as heat to the environment. The time in which 63% $(1-e^{-1})$ of the *z*-component of the magnetization is restored is called T_1 and can be measured by pulse EPR using the sequence $\pi - t - (\pi/2) - \tau - \pi - \tau -$ [echo], where t is the increment time and τ is the delay time.

Transverse relaxation causes the decay of $\vec{\mathrm{M}}$ in the transversal (*xy*) plane. In contrast to longitudinal relaxation, the transversal relaxation does not lead to a loss of magnetic energy of the spins. The time in which the *x*- (or *y*-) component of the magnetization decays to 37% is called T_2 and can be measured by the pulse sequence $(\pi/2) - \tau - \pi - \tau -$ [echo].

Measurement of T_1 and T_2 by microwave saturation

Pulse measurements may not always be feasible to measure the T_1 and T_2 of a sample. An alternative is offered by microwave saturation, which was recognized in early studies by Portis[20] and Castner[21]. A saturation curve is obtained in cw mode by measuring the amplitude Y of a first-derivative EPR line (Figure 1.7) as a function of the microwave power P. At low microwave power Y increases linearly with $\sqrt{P}$, while Y decreases for higher microwave powers. The loss of amplitude at higher microwave power results from saturation. Figure 1.8 shows an example of a saturation curve. The value $P_{1/2}$ is characteristic for a saturation curve and is defined as the microwave power, at which Y is half of the unsaturated value. The shape of the saturation curve is, amongst others, determined by the product T_1T_2 [22]:

$$Y \propto \frac{B_1}{\left(1+B_1^2\gamma^2T_1T_2\right)^{\varepsilon}}, \tag{1.8}$$

where B_1 is the microwave magnetic field, $\gamma = g_e\mu_B/\hbar$, and ε is a measure for the homogeneity of the saturation. For a homogeneously broadened (Lorentzian) line, $\varepsilon = 1.5$. For an inhomogeneously broadened (Gaussian) line, $\varepsilon = 0.5$. Measurement of the amplitude Y as a function of microwave power (B_1^2) allows the determination of the product of T_1 and T_2.

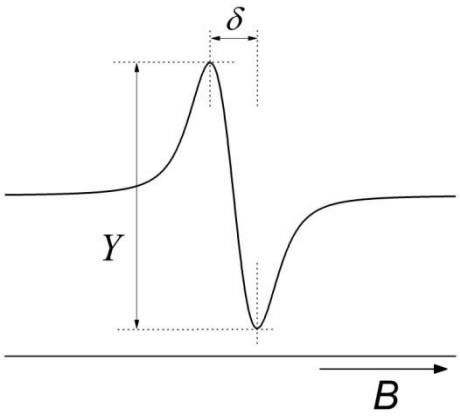

Figure 1.7 First-derivative EPR line with a peak-to-peak amplitude *Y* and a peak-to-peak linewidth δ.

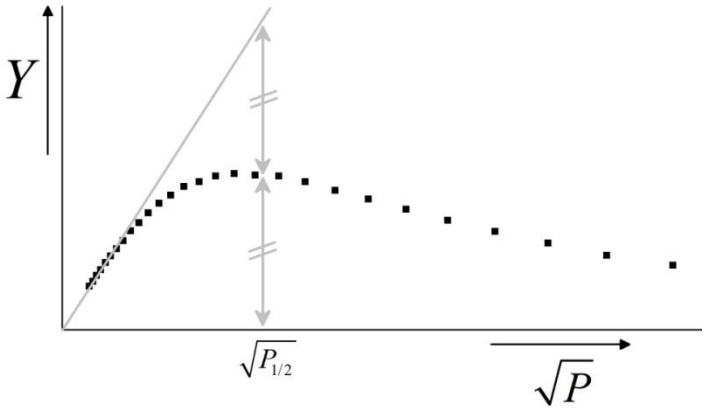

Figure 1.8 An example of a saturation curve. At low microwave power, Y increases linearly with $\sqrt{P}$. At higher microwave powers, saturation occurs, causing Y to decrease. The value $P_{1/2}$ is defined as the microwave power at which Y is half of the unsaturated value.

1.4 Spin-spin interactions

Spin-spin interactions are detected by EPR, if two unpaired electrons, at sites A and B, are sufficiently close. Hence, spin-spin interactions may serve as indication for the proximity of the electrons. Two terms in spin-spin

interactions are distinguished: exchange interaction and dipole-dipole interaction.

Exchange interaction

Exchange interaction arises from the overlap between electronic wavefunctions. The exchange Hamiltonian is

$$\mathcal{H}_e = -2J\vec{\mathrm{S}}_{\mathrm{A}} \cdot \vec{\mathrm{S}}_{\mathrm{B}}, \tag{1.9}$$

where J is the exchange energy. The eigenfunctions of $\mathcal{H}_e$ are the S = 0 (singlet) and S = 1 (triplet) spin functions, where S refers to the total spin of the two electrons.

We shall consider the regime of fast molecular tumbling. Additionally, we take into account the Zeeman interaction and the hyperfine interaction of the electron spins with two ^{14}N nuclear spins (I = 1). The eigenvalues of the singlet and the three triplet spin functions are

$$\begin{array}{lcl} \text{(triplet)} & \left|\beta_{\mathrm{A}}\beta_{\mathrm{B}}\right\rangle & \frac{1}{4}J + g\mu_B B + \frac{1}{2}aM_I \\ \text{(triplet)} & \frac{1}{\sqrt{2}}\left|\alpha_{\mathrm{A}}\beta_{\mathrm{B}} + \beta_{\mathrm{A}}\alpha_{\mathrm{B}}\right\rangle & -\frac{1}{4}J + \frac{1}{2}\sqrt{a^2\left(\Delta m_i\right)^2 + J^2} \\ \text{(singlet)} & \frac{1}{\sqrt{2}}\left|\alpha_{\mathrm{A}}\beta_{\mathrm{B}} - \beta_{\mathrm{A}}\alpha_{\mathrm{B}}\right\rangle & -\frac{1}{4}J - \frac{1}{2}\sqrt{a^2\left(\Delta m_i\right)^2 + J^2} \\ \text{(triplet)} & \left|\alpha_{\mathrm{A}}\alpha_{\mathrm{B}}\right\rangle & \frac{1}{4}J - g\mu_B B - \frac{1}{2}aM_I \end{array} \tag{1.10}$$

with

$$M_I = m_i^{\mathrm{A}} + m_i^{\mathrm{B}} \quad \text{and} \quad \Delta m_i = m_i^{\mathrm{A}} - m_i^{\mathrm{B}}. \tag{1.11}$$

The total quantum number M_I splits up the state $|\alpha_A\alpha_B\rangle$ and $|\beta_A\beta_B\rangle$ into five levels $(M_I = -2, -1, 0, +1, +2)$. The square of the difference in nuclear quantum numbers $(\Delta m_i)^2$ splits up the states $\frac{1}{\sqrt{2}}|\alpha_A\beta_B + \beta_A\alpha_B\rangle$ and $\frac{1}{\sqrt{2}}|\alpha_A\beta_B - \beta_A\alpha_B\rangle$ into three levels $(|\Delta m_i| = 0, 1, 2)$. With the selection rule $\Delta m_s = \pm 1$, the allowed transitions are:

$$\begin{aligned}
\tfrac{1}{\sqrt{2}}|\alpha_A\beta_B + \beta_A\alpha_B\rangle &\leftrightarrow |\beta_A\beta_B\rangle \quad h\nu = \tfrac{1}{2}J + g\mu_B B + \tfrac{1}{2}aM_I - \tfrac{1}{2}\sqrt{a^2(\Delta m_i)^2 + J^2} \\
\tfrac{1}{\sqrt{2}}|\alpha_A\beta_B + \beta_A\alpha_B\rangle &\leftrightarrow |\alpha_A\alpha_B\rangle \quad h\nu = -\tfrac{1}{2}J + g\mu_B B + \tfrac{1}{2}aM_I + \tfrac{1}{2}\sqrt{a^2(\Delta m_i)^2 + J^2} \\
\tfrac{1}{\sqrt{2}}|\alpha_A\beta_B - \beta_A\alpha_B\rangle &\leftrightarrow |\beta_A\beta_B\rangle \quad h\nu = \tfrac{1}{2}J + g\mu_B B + \tfrac{1}{2}aM_I + \tfrac{1}{2}\sqrt{a^2(\Delta m_i)^2 + J^2} \\
\tfrac{1}{\sqrt{2}}|\alpha_A\beta_B - \beta_A\alpha_B\rangle &\leftrightarrow |\alpha_A\alpha_B\rangle \quad h\nu = -\tfrac{1}{2}J + g\mu_B B + \tfrac{1}{2}aM_I - \tfrac{1}{2}\sqrt{a^2(\Delta m_i)^2 + J^2}
\end{aligned} \tag{1.12}$$

In the weak exchange regime, i.e., for $|J| \ll a$, the four equations in equation 1.12 reduce to the form of equation 1.6, which is the resonance condition for non-interacting electron spins. A three-line spectrum, such as shown in Figure 1.4, results.

In the strong exchange regime, i.e., for $|J| \gg a$, the term $\frac{1}{2}\sqrt{a^2(\Delta m_i)^2 + J^2}$ in equation 1.12 reduces to $\frac{1}{2}J$. In this regime the singlet-triplet transitions are forbidden and the allowed triplet-triplet transitions occur for

$$h\nu = g\mu_B B + \tfrac{1}{2}aM_I . \tag{1.13}$$

Figure 1.9 shows the energy levels and the triplet-triplet transitions for two electron spins in the strong exchange regime. Owing to different combinations of m_i^A and m_i^B the energy levels of states $|\alpha_A\alpha_B\rangle$ and $|\beta_A\beta_B\rangle$ are one-, two-,

three-, two-, and one-fold degenerate. Therefore, the spectrum contains five lines, which have 1:2:3:2:1 relative line amplitudes (Figure 1.10). The spectral lines are spaced by $\frac{1}{2}a$.

More complex spectra are expected for systems in the intermediate exchange regime, i.e., for $|J| \sim a$.

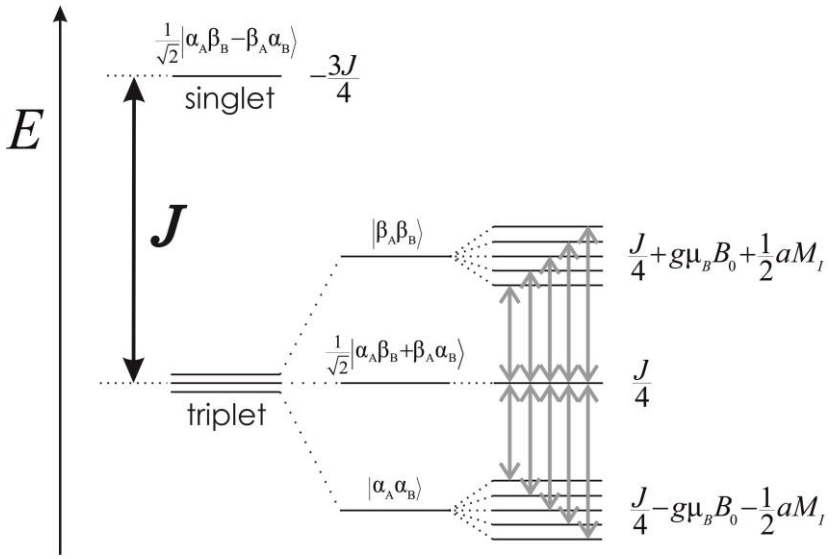

Figure 1.9 Schematic energy diagram of two electron spins (in singlet and triplet state) in the strong exchange regime. The degree of coupling between the electron spins is given by the exchange energy (J). Also, the effect is shown of electron spins interacting with an external magnetic field and with a ^{14}N nuclear spin (I = 1). The grey arrows indicate the allowed triplet-triplet transitions.

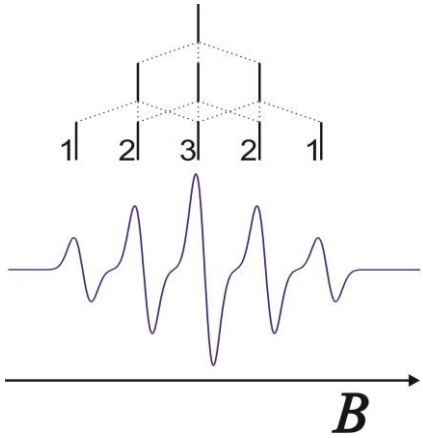

Figure 1.10 An example of a cw-EPR spectrum containing five lines as a result of two interacting electron spins in the strong exchange regime, coupled to two I = 1 nuclei. The EPR lines have 1:2:3:2:1 relative amplitudes and correspond to the transitions depicted in the energy diagram of Figure 1.9.

Dipole-dipole interaction

The dipole-dipole coupling ω_{dd} between two spins (g values g_1 and g_2) is proportional to the inverse cube of the distance r and is given by[13]

$$\omega_{dd}(\theta, r) = \frac{2\pi g_1 g_2}{g_e^{\,2}}(3\cos^2\theta - 1)\frac{52.04}{r^3}\left[\text{MHz nm}^3\right], \qquad (1.14)$$

where g_e is the g value of the free electron. The angle θ is the angle of the spin-spin vector and the magnetic field. For distances up to about 2 nm, dipolar broadening in cw spectra allows for a distance determination by lineshape analysis[24]. Pulse EPR-techniques[23] can access distances in the range of 2 – 6 nm or, in favourable cases, even up to 8 nm[13;25].

To determine distances larger than 2 nm, the most widely used technique is the four-pulse double electron-electron resonance (DEER) experiment[26]. This experiment consists of the pulse sequence

$(\pi/2)_{obs} - \tau_1 - (\pi)_{obs} - (\tau_1 + t) - (\pi)_{pump} - (\tau_2 - t) - (\pi)_{obs} - \tau_2 -$ [echo],

where the subscripts *obs* and *pump* indicate pulses occurring at the observer

and pump frequency. The sequence is illustrated in Figure 1.11a. The measured DEER trace (Figure 1.11b) can be analysed with the proper software[27] to convert the time-domain signal into a distance distribution (Figure 1.11c).

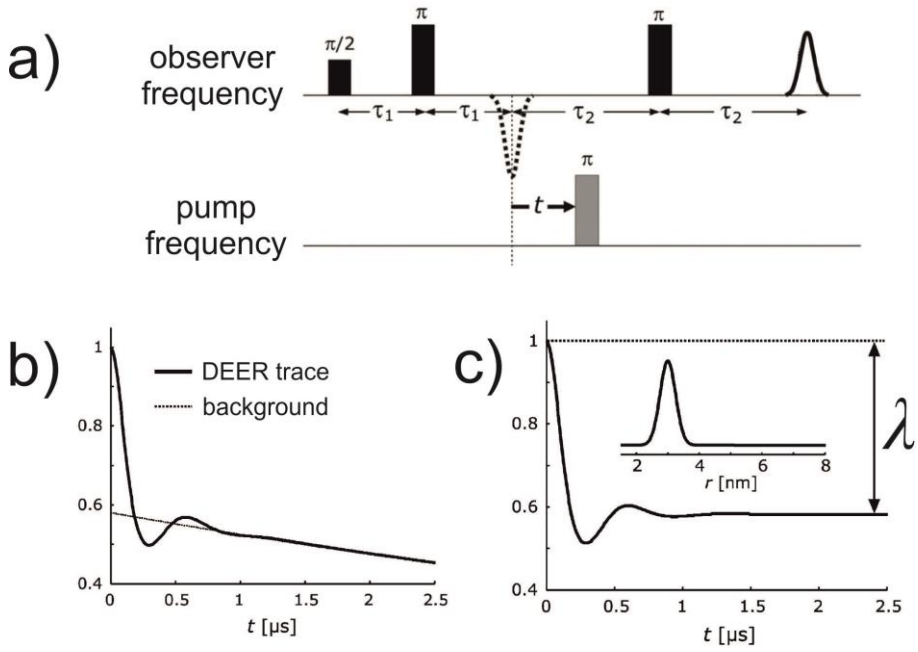

Figure 1.11 The DEER experiment and data analysis. a) The DEER experiment is achieved by a four-pulse sequence at two frequencies that are ~ 65 MHz apart. Delay times τ_1 and τ_2 are kept fixed, while delay time t between the unobserved first echo (dotted line) and the pump pulse is varied. b) The measured DEER trace is the integrated intensity of the observed echo as a function of the dipolar evolution time t. The trace contains a modulation, which is the result of the dipolar coupling between two electron spins. Once the DEER trace is corrected for the background, c) the modulation can be transformed into a distance distribution, which, for this trace, is shown in the inset. The modulation depth (λ) is related to the number of spins that account for the measured DEER trace. The figures concern an edited version of those in reference [25].

1.5 Scope of thesis

This section gives a brief overview of the subjects studied in this work.

In *Chapter 2*, continuous-wave EPR at 9 GHz is used to study the complex formation of E and K peptides, which mimic essential parts of proteins that facilitate membrane fusion. The spectral changes upon mixing of the E and K peptides show that the heterodimer formation can indeed be detected by EPR.

In *Chapter 3*, all three experimental EPR frequencies available at Leiden Institute of Physics (9, 94, and 275 GHz) are used to study the complex of cytochrome *c* peroxidase with spin-labelled cytochrome *c*. The combination of EPR measurements, spectral simulations and principal component analysis allows for a quantative analysis of the immobilization of the spin label upon complex formation of the proteins.

In *Chapter 4*, microwave-power saturation is used to study the relaxation behaviour of the paramagnetic centre of TOAC in doubly labelled 3_{10}-helical peptides. This work demonstrates that in the doubly labelled peptides the exchange interaction J causes additional relaxation of the paramagnetic centres compared to mono-labelled peptides.

In *Chapter 5*, the unfolding of a doubly labelled protein is studied by the four-pulse DEER experiment. A folding intermediate is revealed by the analysis of the distance distributions.

References

[1] www.rcsb.org/pdb/statistics/contentGrowthChart.do?content=total&seqid=100

[2] L. Pauling, R.B. Corey, H.R. Branson, The Structure of Proteins - 2 Hydrogen-Bonded Helical Configurations of the Polypeptide Chain. Proceedings of the National Academy of Sciences of the United States of America **37** (1951) 205-211.

[3] F.H.C. Crick, The Packing of Alpha-Helices - Simple Coiled-Coils. Acta Crystallographica **6** (1953) 689-697.

[4] J.D. Watson, F.H.C. Crick, Molecular Structure of Nucleic Acids - A Structure for Deoxyribose Nucleic Acid. Nature **171** (1953) 737-738.

[5] R.E. Franklin, R.G. Gosling, Molecular Configuration in Sodium Thymonucleate. Nature **171** (1953) 740-741.

[6] N.M. Atherton, Principles of electron spin resonance, Ellis Horwood, Chichester, 1993.

[7] S.I. Ohnishi, H.M. McConnell, Interaction of Radical Ion of Chlorpromazine with Deoxyribonucleic Acid. Journal of the American Chemical Society **87** (1965) 2293.

[8] T.J. Stone, T. Buckman, P.L. Nordio, H.M. McConnell, Spin-Labeled Biomolecules. Proceedings of the National Academy of Sciences of the United States of America **54** (1965) 1010-1017.

[9] L.J. Berliner, Spin labeling: Theory and Applications, Academic Press, New York, 1976.

[10] L.J. Berliner, J. Grunwald, H.O. Hankovszky, K. Hideg, A Novel Reversible Thiol-Specific Spin Label - Papain Active-Site Labeling and Inhibition. Analytical Biochemistry **119** (1982) 450-455.

[11] A. Rassat, P. Rey, Nitroxides .23. Preparation of Amino-Acid Free Radicals and Their Complex Salts. Bulletin de la Societe Chimique de France (1967) 815-818.

[12] C.J. Lopez, S. Oga, W.L. Hubbell, Mapping Molecular Flexibility of Proteins with Site-Directed Spin Labeling: A Case Study of Myoglobin. Biochemistry **51** (2012) 6568-6583.

[13] G. Jeschke, Distance measurements in the nanometer range by pulse EPR. Chemphyschem **3** (2002) 927-932.

[14] W.L. Hubbell, C. Altenbach, Investigation of Structure and Dynamics in Membrane-Proteins Using Site-Directed Spin-Labeling. Current Opinion in Structural Biology **4** (1994) 566-573.

[15] C. Altenbach, S.L. Flitsch, H.G. Khorana, W.L. Hubbell, Structural Studies on Transmembrane Proteins .2. Spin Labeling of Bacteriorhodopsin Mutants at Unique Cysteines. Biochemistry **28** (1989) 7806-7812.

[16] P. Zeeman, The Effect of Magnetisation on the Nature of Light Emitted by a Substance. Nature **55** (1897) 347.

[17] sites.google.com/site/altenbach/labview-programs/epr-programs/

[18] D.E. Budil, S. Lee, S. Saxena, J.H. Freed, Nonlinear-least-squares analysis of slow-motion EPR spectra in one and two dimensions using a modified Levenberg-Marquardt algorithm. Journal of Magnetic Resonance Series A **120** (1996) 155-189.

[19] S. Stoll, A. Schweiger, EasySpin, a comprehensive software package for spectral simulation and analysis in EPR. Journal of Magnetic Resonance **178** (2006) 42-55.

[20] A.M. Portis, Electronic Structure of F-Centers - Saturation of the Electron Spin Resonance. Physical Review **91** (1953) 1071-1078.
[21] T.G. Castner, Saturation of the Paramagnetic Resonance of A V-Center. Physical Review **115** (1959) 1506-1515.
[22] C.P. Poole, Electron Spin Resonance, Wiley, New York, 1983.
[23] G. Jeschke, Determination of the nanostructure of polymer materials by electron paramagnetic resonance spectroscopy. Macromolecular Rapid Communications **23** (2002) 227-246.
[24] A. Schweiger, G. Jeschke Principles of pulse electron paramagnetic resonance, Oxford University Press, New York, 2001.
[25] G. Jeschke, Y. Polyhach, Distance measurements on spin-labelled biomacromolecules by pulsed electron paramagnetic resonance. Physical Chemistry Chemical Physics **9** (2007) 1895-1910.
[26] M. Pannier, S. Veit, A. Godt, G. Jeschke, H.W. Spiess, Dead-time free measurement of dipole-dipole interactions between electron spins. Journal of Magnetic Resonance **142** (2000) 331-340.
[27] G. Jeschke, V. Chechik, P. Ionita, A. Godt, H. Zimmermann, J. Banham, C.R. Timmel, D. Hilger, H. Jung, DeerAnalysis2006 - a comprehensive software package for analyzing pulsed ELDOR data. Applied Magnetic Resonance **30** (2006) 473-498.